Atomistic Investigation of Low-Field Mobility in Graphene Nanoribbons

Alessandro Betti, Gianluca Fiori, and Giuseppe Iannaccone, *Senior Member, IEEE*

***Abstract*—We have investigated the main scattering mechanisms affecting the mobility in graphene nanoribbons using detailed atomistic simulations. We have considered carrier scattering due to acoustic and optical phonons, edge roughness, single defects, and ionized impurities, and we have defined a methodology based on simulations of statistically meaningful ensembles of nanoribbon segments. Edge disorder heavily affects the mobility at room temperature in narrower nanoribbons, whereas charged impurities and phonons are hardly the limiting factors. Results are favorably compared with the few experiments available in the literature.**

***Index Terms*—Defects, edge roughness, graphene nanoribbons, impurities, low-field mobility, phonons, scattering.**

I. Introduction

TWO-DIMENSIONAL graphene sheets have demonstrated really attractive electrical properties such as high carrier mobility [1], [2] and large coherence length [3]. However, the experimental data of mobility available in the literature show huge dispersion, ranging from 10^2 to 10^4 cm^2/Vs at room temperature, signaling that the fabrication process is still poorly optimized and not fully repeatable. To guide the process optimization, an exhaustive interpretation of physical mechanisms limiting the mobility would be extremely useful. For graphene nanoribbons (GNRs), a comprehensive experimental characterization of the mobility is still lacking, mainly due to the difficulty in patterning in a repeatable way very narrow ribbons. Few recent interesting experiments are reported in [4] and [5]. GNRs may also suffer the significant degradation of mobility due to additional scattering mechanism, such as edge roughness.

The single most important aspect that makes graphene interesting for nanoscale electronics is its very high mobility. It is therefore of paramount importance to understand if nanostructured graphene can also preserve the high mobility (often) measured in graphene sheets, much larger than that of conventional semiconductors. In addition, one would need to understand the effect on the mobility of different options for graphene functionalization, which could be required to open a semiconducting gap in graphene.

In the current situation, theoretical investigations [6], [7] and numerical simulations [8]–[10] can represent a useful tool to assess the relative impact of different sources of nonidealities on mobility and, consequently, on device performance to provide guidelines for the fabrication process and a realistic evaluation of the perspectives of graphene in nanoelectronics.

An analytical method and a Monte Carlo approach, for example, have been adopted in order to study line-edge roughness (LER) and phonon scattering-limited mobility in [6] and [7], respectively. However, due to the reduced width of the considered devices, effects at the atomistic scale are relevant; therefore, accurate simulation approaches such as semiempirical tight binding are needed.

In this paper, we present atomistic simulations of GNR field-effect transistors (FETs), considering GNR widths ranging from 1 to 10 nm and including scattering due to LER, single defects, ionized impurities, and acoustic and optical phonons. A direct comparison with recently fabricated devices [4] will also be performed. Statistical simulations performed on a large ensemble of nanoribbons with different occurrences of the spatial distribution of nonidealities show that phonons, LER, and defect scattering can likely explain the few available experimental data [4], where the mobility is down to the level of mundane semiconductors (order of $10^2 - 10^3$ cm^2/Vs).

II. Methodology

A long GNR-FET channel, where the mobility is properly defined, is given by a series of N GNR segments of length L such as those we have considered in the simulation (see Fig. 1). For the ith GNR segment, resistance $R_i = V_{\rm DS}/I_i$ is the sum of two contributions, i.e., the channel resistance $R_{{\rm ch},i}$ and the contact (ballistic) resistance $R_B = V_{\rm DS}/I_B$ ($R_i = R_{{\rm ch},i} + R_B$), where $V_{\rm DS}$ is the drain-to-source voltage, whereas I_i and I_B are the total current and the ballistic current in the ith segment, respectively. Assuming that the phase coherence is lost at the interface between segments, resistance $R_{\rm tot}$ of the long channel

Manuscript received August 6, 2010; revised November 27, 2010; accepted December 5, 2010. Date of publication January 31, 2011; date of current version August 24, 2011. This work was supported in part by the European Commission Seventh Framework Program (EC 7FP) through the Network of Excellence Silicon-based nanostructures and nanodevices for long term microelectronics applications under Contract 216171 and the Graphene-based Nanoelectronic Devices project under Contract 215752, by the Ministero dell'Istruzione, dell'Università e della Ricerca through the project "Modeling and simulation of graphene nanoribbon FETs for high-performance and low-power logic applications" (GRANFET, Prot. 2008S2CLJ9), by the European Science Foundation EUROCORES Programme Fundamentals of Nanoelectronics, through funding from the Consiglio Nazionale delle Ricerche (awarded to Istituto di Elettronica e di Ingegneria dell'Informazione e delle Telecomunicazioni-PISA) and the European Commission Sixth Framework Programme, under Project Dewint (Contract ERAS- CT-2003-980409). The review of this paper was arranged by Editor R. Huang.

The authors are with the Dipartimento di Ingegneria dell'Informazione: Elettronica, Informatica, Telecomunicazioni, Università di Pisa, 56100 Pisa, Italy (e-mail: alessandro.betti@iet.unipi.it; g.iannaccone@iet.unipi.it; gfiori@mercurio.iet.unipi.it).

Color versions of one or more of the figures in this paper are available online at http://ieeexplore.ieee.org.

Digital Object Identifier 10.1109/TED.2010.2100045

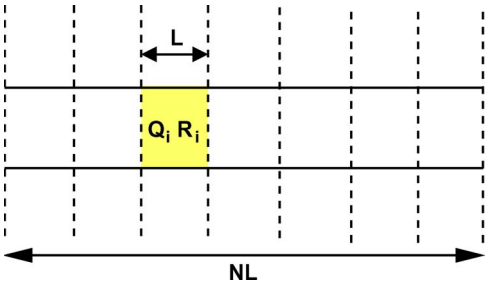

Fig. 1. GNR-FET channel with length NL and the simulated GNR segment with length L.

GNR is therefore the sum of N channel resistances and one contact resistance, i.e.,

$$R_{\rm tot} = \left(\sum_{i=1}^{N} R_{{\rm ch},i}\right) + R_B = N\langle R\rangle - (N-1)R_B \qquad (1)$$

where $\langle R\rangle = (1/N)\sum_{i=1}^{N} R_i$ is the mean resistance evaluated on the ensemble of nanoribbon segments. Therefore, the mobility of a long channel would read

$$\mu_n = \frac{L_{\rm tot}^2\, G_{\rm tot}}{Q_{\rm tot}} = \frac{L_{\rm tot}^2}{Q_{\rm tot}} \frac{1}{N\langle R\rangle - (N-1)R_B} \qquad (2)$$

where index n denotes each type of scattering mechanism limiting the mobility (defects, edge roughness, or impurities), $L_{\rm tot} = NL$ is the total GNR length, $Q_{\rm tot} = \sum_{i=1}^{N} Q_i = N\langle Q\rangle$ is the total charge in the channel, and $\langle Q\rangle$ is the mean mobile charge in a segment.

For large values of N, one can discard 1 with respect to N in (2) so that we obtain the formula that we use in this paper [11]

$$\mu_n = \frac{L^2}{(\langle R\rangle - R_B)\langle Q\rangle}. \qquad (3)$$

The root mean squared error of mobility σ_μ has been computed by means of a Taylor expansion up to the first order of (3) with respect to statistical fluctuations of resistance $R = R_{\rm ch} + R_B$, i.e.,

$$\Delta\mu = \left|\frac{\partial\mu}{\partial R}\right| \Delta R = \frac{L^2}{\langle Q\rangle} \frac{\Delta R}{(\langle R\rangle - R_B)^2} = \mu \frac{\Delta R}{\langle R\rangle - R_B} \qquad (4)$$

and therefore

$$\sigma_\mu^2 = \left(\frac{\mu}{\langle R\rangle - R_B}\right)^2 \sigma_R^2 \qquad (5)$$

where $\Delta R = \sqrt{\sigma_R^2/N}$ and

$$\sigma_R^2 = 1/(N-1)\sum_{i=1}^{N} (R_i - \langle R\rangle)^2 \qquad (6)$$

is the variance of R.

Statistical simulations of the resistance on a large ensemble of nanoribbon segments with different actual distributions of nonidealities have been performed. In particular, mobility μ_n has been computed in the linear-transport regime for large gate voltages V_{GS} and a small drain-to-source bias $V_{\rm DS} = 10$ mV. The mobility has been extracted by means of (3), considering an ensemble of $N = 600$ nanoribbon segments with different disorder realizations for 1.12-nm-wide GNRs. Due to the computational cost, at least 40 nanoribbons segments have been instead simulated for 10.10-nm-wide GNRs.

Statistical simulations of random actual distributions of defects, LER, and ionized impurities have been computed through the self-consistent solution of 3-D Poisson and Schrödinger equations within the nonequilibrium Green's function formalism, with a p_z tight-binding Hamiltonian [10], extensively exploiting our open-source simulator NanoTCAD ViDES [12]. In particular, we have imposed at both ends of the segments null Neumann boundary conditions on the potential and open boundary conditions for the transport equation.

In order to compute the LER-limited mobility $\mu_{\rm LER}$, statistical simulations have been performed, considering a given fraction H of single vacancy defects at the edges. H is defined as the probability for each carbon atom at the edges to be vacant. In practice, each sample of the nanoribbon with edge disorder is randomly generated, assuming that each carbon site at the edges has probability H to be replaced by a vacancy. The null hopping parameter has been imposed in correspondence of a defect at the edge.

Defects have been modeled using the on-site energy and the hopping parameter extracted from discrete-Fourier-transform calculations [13]. In particular, for a fixed defect concentration n_d, each sample of the nanoribbon with defects is randomly generated, assuming that each carbon atom has probability n_d to be replaced by a vacancy.

As previously assumed in *ab initio* calculations [14], we have considered a surface-impurity distribution of positive charges equal to $+0.4\ q$ placed at a distance of 0.2 nm from the GNR surface, where q is the elementary charge. Again, if $n_{\rm IMP}$ is the impurity fraction, a sample with surface impurities is randomly generated by assuming that each carbon atom has probability $n_{\rm IMP}$ to be at 0.2 nm from an impurity in the dielectric layer.

In Fig. 2(a) and (b), we show the distributions of Q when considering the LER $H = 5\%$ and the defects $n_d = 2.5\%$ for $W = 1.12$ nm. In each picture, we show the mean value $\langle Q\rangle$ and the standard deviation σ_Q of the random variable Q. For comparison, the corresponding normal distribution is shown.

The phonon-limited mobility $\mu_{\rm ph}$ (both acoustic and optical) has been computed by means of a semianalytical model as in [6] but extending the Kubo–Greenwood formalism beyond the effective-mass approximation and accounting for the energy relaxation at GNR edges [15]. Starting from the Boltzmann transport equation, the phonon-limited mobility for a 1-D conductor can be expressed as [16]

$$\mu_{\rm ph} = -\frac{e}{\hbar}\sum_j \left\langle \tau_{{\rm P}j}\, v_{{\rm x}j}\, \frac{\partial f(k_x)}{\partial k_x}\, \frac{1}{f(k_x)} \right\rangle \qquad (7)$$

where $v_{{\rm x}j} = (1/\hbar)\, dE_j/dk_x$ is the electron velocity in the longitudinal direction x for the jth electron subband and $\tau_{{\rm P}j}$ is the corresponding momentum relaxation time for electron–phonon scattering. In (7), $\langle\cdot\rangle$ denotes the expectation value averaged on the Fermi factor f as

$$\langle g\rangle = \frac{2}{n_{1D}} \int_{-\infty}^{+\infty} dk_x\, \frac{1}{2\pi}\, g(k_x)\, f(k_x) \qquad (8)$$

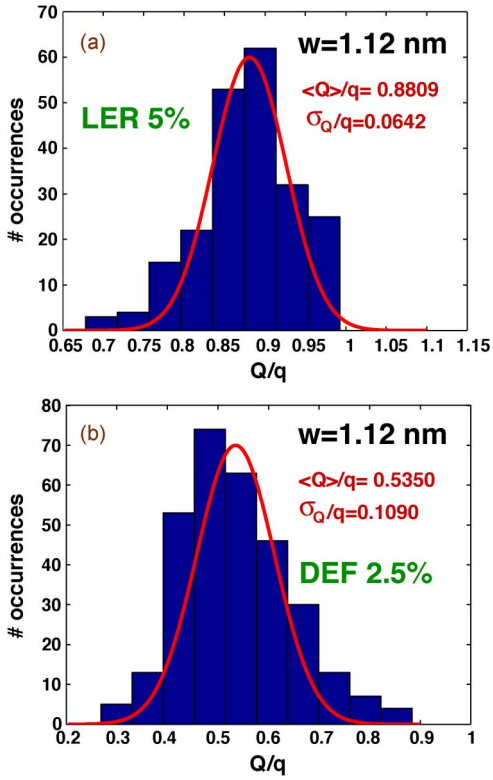

Fig. 2. Distributions of charge Q in each GNR segment ($W = 1.12$ nm) obtained from statistical simulations of random distributions of (a) LER ($H = 5\%$) and (b) defects ($n_d = 2.5\%$).

where n_{1D} is the 1-D carrier density. In order to compute (7), the following electron dispersion curve has been exploited for the jth subband [15]:

$$E_j(k_x) = \sqrt{E_{\mathrm{Cj0}}^2 + E_{\mathrm{Cj0}}\frac{\hbar^2 k_x^2}{m_j}} + E_{\mathrm{Cj}} - E_{\mathrm{Cj0}} \tag{9}$$

where $E_{\mathrm{Cj}} = E_{\mathrm{Cj0}} - q\Phi_C$ is the cutoff energy of the jth subband when the electrostatic channel potential Φ_C is different from zero ($E_{\mathrm{Cj}} = E_{\mathrm{Cj0}}$ for $\Phi_C = 0$ V). According to [15], the effective electron mass m_j on the jth subband reads

$$m_j = -\frac{2}{3}\frac{\hbar^2 E_{\mathrm{Cj0}}}{a^2 t^2 A_j} \tag{10}$$

where t is the graphene hopping parameter (-2.7 eV) and $A_j = \cos(\pi j/(l+1))$, where l is the number of dimer lines of the GNR. For the first conduction subband, $E_{\mathrm{Cj0}} = E_g/2$, where E_g is the energy gap and j (which runs from 1 to l) is the index for which A_j is closest to $-1/2$.

The corresponding density of states, accounting for the energy relaxation at outermost layers of the GNR [15], reads

$$\rho_{1\mathrm{Dj}}(E) = \frac{2}{\pi\hbar}\sqrt{\frac{m_j(E + E_{\mathrm{Cj0}} - E_{\mathrm{Cj}})^2}{|E_{\mathrm{Cj0}}(E - E_{\mathrm{Cj}})(E + 2E_{\mathrm{Cj0}} - E_{\mathrm{Cj}})|}}. \tag{11}$$

By means of (9) and (11), the phonon-limited mobility of a 1-D conductor [see (7)] can be expressed as the sum over all contributing subbands j [17], i.e.,

$$\mu_{\mathrm{ph}} = \frac{2q}{\pi\hbar n_{2D} W k_B T}\sum_j \int_{E_{\mathrm{Cj}}}^{+\infty} dE\, \tau_{\mathrm{Pj}}(E)\frac{f(E)\,[1 - f(E)]}{E - E_{\mathrm{Cj}} + E_{\mathrm{Cj0}}} \times \left(\frac{E_{\mathrm{Cj0}}}{m_j}\left[(E - E_{\mathrm{Cj}} + E_{\mathrm{Cj0}})^2 - E_{\mathrm{Cj0}}^2\right]\right)^{1/2} \tag{12}$$

where $n_{2D} = n_{1D}/W$ is the total 2-D electron density, W is the GNR width, and T is the temperature.

For what concerns longitudinal phonons, scattering rates are evaluated as in [6]. According to [6], only intrasubband scattering has been considered. In particular, the longitudinal optical (LO) phonon scattering rate reads as

$$1/\tau_{\mathrm{OP}}(E) = \frac{n^{\mp}\pi D_{\mathrm{OP}}^2}{4\rho W\omega_{\mathrm{LO}}}\rho_{1\mathrm{Dj}}(E \pm \hbar\omega_{\mathrm{LO}}) \times (1 + \cos\theta_{\mathbf{k},k'})\frac{1 - f(E \pm \hbar\omega_{\mathrm{LO}})}{1 - f(E)} \tag{13}$$

where $n^- = 1/[\exp(\hbar\omega_{\mathrm{LO}}/k_B T) - 1]$ is the Bose–Einstein occupation factor and $n^+ = n^- + 1$, $\hbar\omega_{\mathrm{LO}}$ is the optical-phonon energy, D_{OP} is the optical deformation potential, and $\rho = 7.6 \times 10^{-8}$ g/cm^2 is the 2-D density of graphene. Factor $(1 + \cos\ \theta_{\mathbf{k},\mathbf{k}'})$ arises from the spinor nature of the graphene eigenfunctions, and $\theta_{\mathbf{k},\mathbf{k}'} = \theta_j - \theta_{j'}$, where $\theta_j = \mathrm{arctg}\ (k_x/k_{\mathrm{yj}})$. Here, k_x (k_x') indicates the initial (final) longitudinal electron wave vector referred to the Dirac point, whereas $k_{\mathrm{yj}} = 2\pi j/[(l+1)a]$ and $k_{\mathrm{yj}'}$ (which is equal to k_{yj} for intrasubband scattering) are the quantized initial and final transverse wave vectors, respectively, where a is the graphene lattice constant, l is the number of dimer lines, and $j = 1, \ldots, l$. The intravalley longitudinal acoustic (LA) phonon scattering rate can be expressed as

$$1/\tau_{\mathrm{ACj}}(E) = \frac{n_{\mathrm{ph}}\pi D_{\mathrm{AC}}^2 q_x}{4\rho W v_S}\rho_{1\mathrm{Dj}}(E)(1 + \cos\theta_{\mathbf{k},\mathbf{k}'}) \tag{14}$$

where $n_{\mathrm{ph}} = n^+ + n^-$, D_{AC} is the deformation potential for acoustic phonons, $v_S = 2 \times 10^4$ m/s is the sound velocity in graphene, and $|q_x| = 2|k_x|$ is the module of the phonon wave vector under the backscattering condition.

For both acoustic and optical phonons, we have considered the four lowest subbands. The electron momentum relaxation time τ_{Pj} is computed by adding the relaxation rate due to the electron scattering with acoustic and optical phonons [17]. As a final remark, the effective mobility, including all types of scattering sources, has been extracted by means of Mathiessen's rule, i.e., $1/\mu_{\mathrm{tot}} = 1/\mu_{\mathrm{LER}} + 1/\mu_d + 1/\mu_{\mathrm{IMP}} + 1/\mu_{\mathrm{ph}}$, where μ_d and μ_{IMP} are the defect- and impurity-limited mobilities, respectively. We have verified the validity of Mathiessen's rule, considering samples with more sources of nonidealities (i.e., LER, ionized impurities, and defects) at the same time. Then, we have compared the computed mobility with that obtained by adding single contributions with Mathiessen's rule, observing a relative error smaller than 3%, which lies within the statistical error.

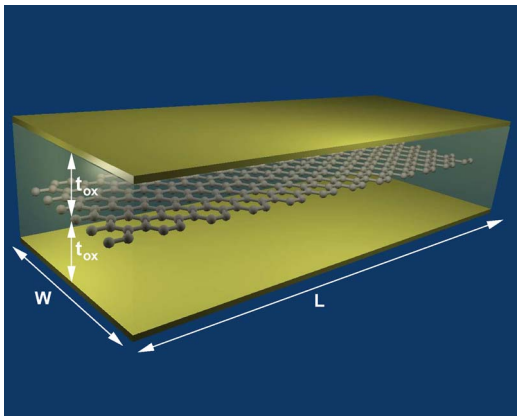

Fig. 3. Three-dimensional structure of the simulated GNR segment.

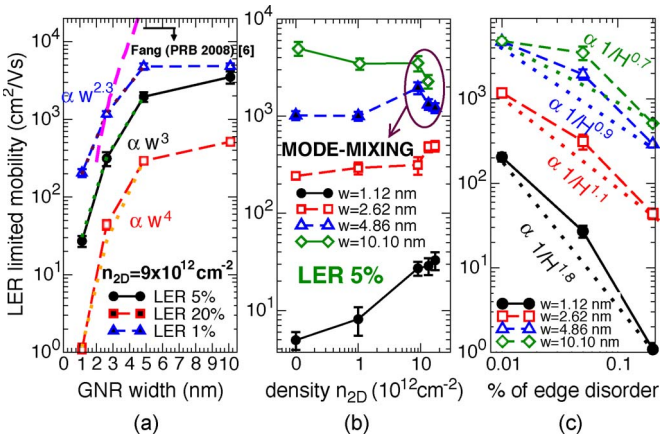

Fig. 4. (a) LER-limited mobility as a function of W for $n_{2D} = 0.9 \times 10^{13}$ cm^{-2} and for different H values. Data extracted from [6] are also reported. (b) LER-limited mobility as a function of n_{2D} for $H = 5\%$. (c) LER-limited mobility as a function of edge disorder concentration H for $n_{2D} = 0.9 \times 10^{13}$ cm^{-2} and for different GNR widths W.

III. Results and Discussions

The simulated segment is a double-gate GNR, embedded in SiO_2 with an oxide thickness t_{ox} of 2 nm, which is 10 nm long (see Fig. 3). The segment length has been chosen to satisfy the assumption of the loss of phase coherence at the segment ends. Indeed, according to recent experiments [18], the phase-coherence length is close to 11 nm in graphene. From a computational point of view, different widths W have been considered, ranging from 1 to 10 nm, i.e., 1.12, 2.62, 4.86, and 10.10 nm. All simulations have been performed at room temperature $T = 300$ K.

A. LER-Limited Mobility

The LER-limited mobility as a function of W for different edge-defect concentrations H is shown in Fig. 4(a) in the above-threshold regime for a 2-D carrier density n_{2D} of 9×10^{12} cm^{-2}. As in all figures in this paper, the error bars represent the estimated root mean squared error σ_μ of the average of the statistical sample (5).

As predicted by the analytical model in [6], $\mu_{\rm LER}$ scales as W^4. Such behavior holds for large H ($\approx$20%) and narrow GNRs ($W < 5$ nm) when scattering from edge defects is expected to be heavier, whereas for wider GNRs and for smaller H, such a law is not obeyed. In particular, for a GNR width larger than 5 nm, $\mu_{\rm LER}$ tends to saturate since the increasing number of subbands contributing to the transport counterbalance the number of final states available for scattering, enhancing the scattering rates. As shown in Fig. 4(b), in narrower GNRs, the higher the electron density, the larger the effective mobility, because of stronger screening. $\mu_{\rm LER}$ decreases for high n_{2D} values and wider GNRs, due to mode mixing, as already observed in silicon nanowire FETs [19]. Indeed, for wider GNRs biased in the inversion regime, more transverse modes are able to propagate in the channel due to the reduced energy separation between different subbands. This leads the edge defects to become a source of intermode scattering, thus reducing $\mu_{\rm LER}$.

Fig. 4(c) shows $\mu_{\rm LER}$ as a function of H, where $\mu_{\rm LER} \propto 1/H$ for wide GNRs, which is consistent with the Drude model and is also observed in graphene in the presence of defects [20]. However, as soon as W decreases, the quantum localization becomes relevant [21], and the Anderson insulator-like behavior [9] is recovered ($\mu_{\rm LER} \propto 1/L^2$) in agreement with analytical predictions [6].

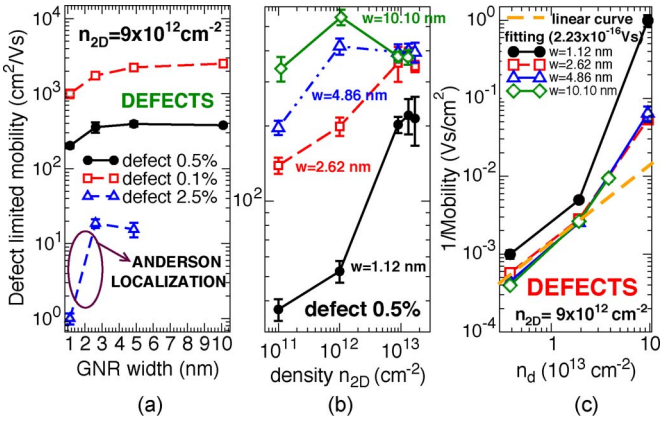

Fig. 5. (a) Defect-limited mobility as a function of W for $n_{2D} = 9 \times 10^{12}$ cm^{-2} and for different defect fractions n_d. (b) Mobility as a function of n_{2D} for a defect fraction $n_d = 0.5\%$. (c) Inverse of the mobility as a function of n_d for $n_{2D} = 9 \times 10^{12}$ cm^{-2} and for different GNR widths W.

B. Defect-Limited Mobility

The defect-limited mobility is plotted in Fig. 5(a) as a function of W for different defect concentrations. Even in this case, the localization affects the mobility in narrower ribbons, particularly for higher n_d (2.5%).

For a fixed defect density, the mobility slightly increases with the electron density due to the larger screening [see Fig. 5(b)], and for larger GNRs biased in the inversion regime, it saturates with increasing W for the same reason discussed above for the LER scattering. In Fig. 5(c), μ_d is plotted as a function of n_d. The wider the ribbons, the closer the mobility follows the simple Drude model ($\mu_d \propto 1/n_d$), as expected for strong disorder and uncorrelated scatterers in 2-D graphene sheets [22]. For $W = 10.10$ nm, atomistic simulations are in agreement with experimental results; a linear-curve fitting ($\mu = C/n_d$) leads to a proportionality factor of 2.23×10^{-16} Vs, similar with

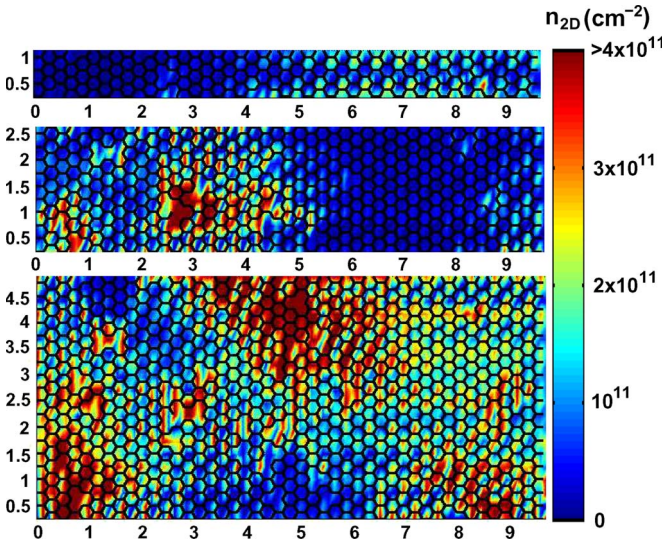

Fig. 6. Carrier density n_{2D} in the GNR channel for different GNR widths. (From top to bottom) $W = 1.12$, 2.62, and 4.86 nm.

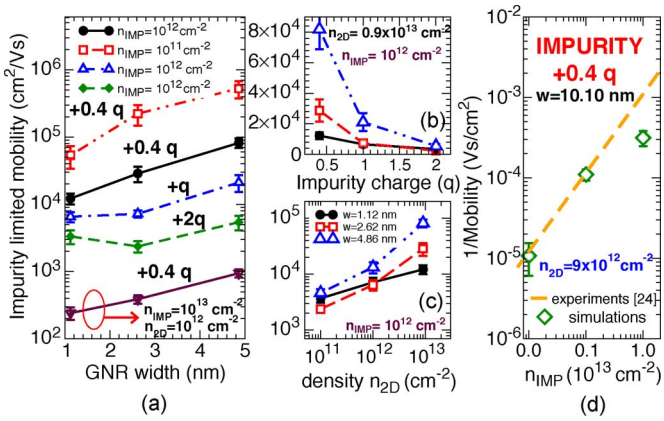

Fig. 7. (a) Impurity-limited mobility as a function of W for different impurity concentrations $n_{\rm IMP}$ and impurity charges. (b) Mobility as a function of the impurity charge for $n_{\rm IMP} = 10^{12}$ cm^{-2} and for different W values. In (a) and (b), $n_{2D} = 0.9 \times 10^{13}$ cm^{-2}, except otherwise specified. (c) Impurity-limited mobility as a function of n_{2D} for different W values ($n_{\rm IMP} = 10^{12}$ cm^{-2} and the impurity charge is $+0.4q$). (d) Inverse mobility as a function of $n_{\rm IMP}$ for $W = 10.10$ nm. The carrier density is $n_{2D} = 0.9 \times 10^{13}$ cm^{-2}. The experimental slope 2×10^{-16} Vs extracted in [24] is also reported.

those extracted in the case of Ne^+ and He^+ irradiated graphene samples (7.9×10^{-16} and 9.3×10^{-16} Vs, respectively) [20].

In Fig. 6, the GNR carrier density for widths ranging from 1.12 to 4.86 nm is shown. As can be seen in Fig. 6, the Anderson localization strongly degrades the electron mobility [21], creating percolating paths in wider GNRs and blocking the conduction in the narrower ones.

C. Ionized-Impurity-Limited Mobility

The impurity-limited mobility $\mu_{\rm IMP}$, as a function of W, is shown in Fig. 7(a) for $n_{2D} = 9 \times 10^{12}$ cm^{-2} and for different impurity charge concentrations. As can be noted, even a high impurity concentration of 10^{12} cm^{-2} yields large mobility for a $0.4q$ impurity charge. However, no indications are present in literature regarding the amount of the unintentional doping charge [23], [24]. Therefore, in order to also check the effect of the impurity ionization on the electron transport, statistical simulations have been performed by increasing the impurity charge up to $+2q$. The mobility as a function of the impurity charge is plotted in Fig. 7(b) for different W and for $n_{2D} = 9 \times 10^{12}$ cm^{-2}. In this case, smaller values of μ (1700 cm^2/Vs) are obtained for very narrow GNRs due to the strongly nonlinear impact on screening in the channel. Even in this case, the localization strongly degrades the mobility for narrower ribbons.

To further test the importance of unintentional doping in limiting the mobility, we have considered excess charge densities up to 10^{13} cm^2, which have been encountered in experiments [23]. As shown in Fig. 7(a), in this case, the mobility decreases down to 10^2 cm^2/Vs for narrower GNRs. In Fig. 7(c), the impurity-limited mobility is plotted as a function of n_{2D} for $n_{\rm IMP} = 10^{12}$ cm^{-2} and impurity charge $+0.4q$ and for different W values. According to [25] and [26], $\mu_{\rm IMP}$ in graphene does not depend on the electron density. The behavior is different in GNRs because, up to an electron density of 10^{12} cm^{-2}, only the ground state is occupied so that the size quantum-limit approximation is verified [6], [27]. Since the scattering rate $1/\tau \propto \epsilon^{-2}$ [25] and the static dielectric function ϵ increases with n_{2D} [27], the screening becomes stronger with increasing n_{2D}. As a consequence, $\mu_{\rm IMP} \propto \tau$ in GNRs has the increasing monotonic behavior shown in Fig. 7(c). In Fig. 7(d), we compare experimental results available in literature [24] for graphene, showing the inverse of the impurity-limited mobility as a function of $n_{\rm IMP}$ for $W = 10.10$ nm and by considering an impurity charge of $+0.4q$; as expected, for uncorrelated scatterers, $\mu_{\rm IMP} \propto 1/n_{\rm IMP}$, and as can be seen, experiments and simulations show quite a good agreement.

D. Acoustic- and Optical-Phonon-Limited Mobility

Our paper has been also directed toward the investigation of the impact of phonon scattering, through the Kubo–Greenwood formalism [28], [29]. A wide range of phonon parameter values is currently present in the literature [1], [6], [26], [30] [i.e., acoustic $(D_{\rm AC})$ and optical $(D_{\rm OP})$ deformation potentials, as well as optical-phonon energy $\hbar\omega_{\rm LO}$]. We observe that the most widely used phonon parameters are those adopted in [1], [6], and [31], i.e., $D_{\rm AC} = 16$ eV, $\hbar\omega_{\rm LO} = 160$ meV, and $D_{\rm OP} = 1.4 \times 10^9$ eV/cm, where $\hbar\omega_{\rm LO}$ is the zone-boundary LO phonon energy. Such values have been tested toward those provided in [7], [32], and [33], showing a good agreement as far as the mobility is concerned.

To prove the validity of our approach, we have first compared our results with those obtained by means of an accurate 2-D Monte Carlo simulator [7]. For a fair comparison, the same phonon parameters and the same scattering rates as in [7] have been used. As can be seen in Fig. 8(a), results are in good agreement, particularly for wider GNRs. However, such parameters correspond to the out-of-plane mode ZO, which, according to symmetry-based considerations [34], density functional study [35], and Raman spectroscopy [36], is much weaker than in-plane vibrations.

Therefore, in the following, we adopt the parameters discussed above for the LA and LO phonons, and the scattering rates described in (13) and (14). In Fig. 8(b) the acoustic- and

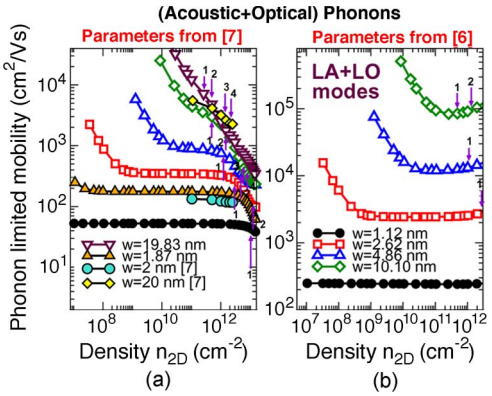

Fig. 8. (a) Mobility limited by phonons (zone-boundary ZO+acoustic) scattering as a function of n_{2D} for different widths W, computed by means of parameters from [7]. Data from [7] are also reported. (b) Same plot of (a), exploiting parameters from [6], corresponding to the zone-boundary LO mode. In both plots, the threshold densities at which the different subbands are activated are sketched.

optical-phonon-limited mobility is shown as a function of n_{2D}. As expected, emission scattering rates are found to be larger than absorption scattering rates due to their higher Bose–Einstein occupation numbers. In addition, as also observed in graphene [37], we have verified that the contribution of optical phonons is also negligible in GNRs and $\mu_{\rm ph}$ is dominated by (intravalley) acoustic-phonon scattering [6], [7] [see Fig. 8(b)]. Note also that, unlike in graphene where $\mu_{\rm ph} \propto 1/n_{2D}$ [38], in GNRs, the transverse confinement leads to a nonmonotonic n_{2D} dependence as in carbon nanotubes [39]. As can be seen, $\mu_{\rm ph}$ slightly increases due to the reduced number of available states for scattering.

We observe that several recent studies [38], [40], [41] have demonstrated that surface phonons of the substrate represent a severe source of scattering, which strongly limits the transport in graphene. However, we expect this effect to be much larger in high-k dielectrics such as HfO_2, rather than in SiO_2, which is the insulator considered in this paper. This issue will be the topic of a more comprehensive work on electron–phonon scattering in GNRs, which is beyond the scope of this paper.

Finally, we compare the total mobility with experiments from Wang *et al.* [4] (see Fig. 9). In particular, we show the mobility limited by different scattering mechanisms, as well as the total mobility computed by means of Mathiessen's rule. As can be seen, when using parameters in [6], the LER is the most-limiting mechanism ($H = 5\%$) for very narrower GNRs, whereas for wider GNRs, the defect scattering is predominant if $n_d = 0.5\%$ is considered. As an additional remark, we have checked that the same conclusion holds even if we consider much lower deformation potentials for phonons, which decrease the impact of phonon scattering, such as those provided in [30].

IV. Conclusion

We have defined a simulation methodology based on atomistic simulations on statistically significant ensembles of GNR segments to understand the functional dependence of the GNR mobility upon different factors and to quantitatively assess the importance of different scattering mechanisms.

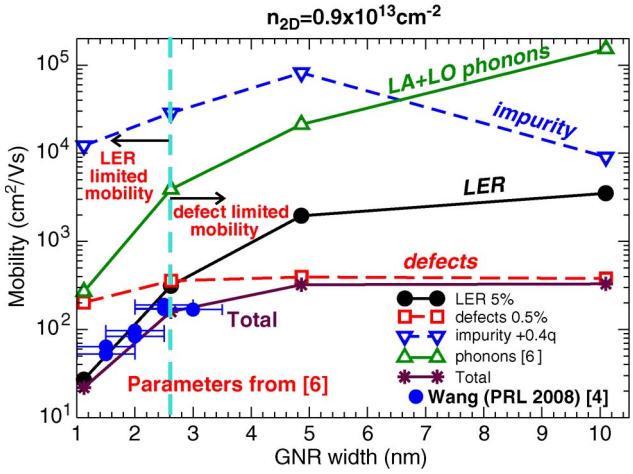

Fig. 9. Mobility limited by phonon, LER, defect, and impurity scattering in the inversion regime for an LER concentration $H = 5\%$ and $n_d = 0.5\%$. The parameters for the scattering rates have been taken from [6]. The experimental mobility from [4] is also reported. $n_{2D} = 0.9 \times 10^{13}$ cm^{-2}. $n_{\rm IMP} = 10^{12}$ cm^{-2}.

We have used such a methodology to investigate the mobility in GNRs of width ranging from 1 to 10 nm. First, we have found that, unlike in 2-D graphene, electron-impurity scattering in GNRs is far too weak to affect the low-field mobility. In addition, using well-established parameters for electron–phonon coupling, we have found that the phonon scattering is hardly the limiting factor of the GNR mobility. For narrower GNRs, the LER is the main scattering mechanism. This result is consistent with the findings in [5], where wider nanoribbons with very rough edges are characterized. Finally, for a fixed defect density or LER, the mobility tends to decrease with the GNR width for narrower devices, suggesting the occurrence of localization effects.

Acknowledgment

The authors would like to thank M. Lemme, P. Palestri, P. Michetti, and T. Fang for useful discussions, and CINECA-Consorzio Interuniversitario Supercomputing Center, Bologna, and www.nanohub.org for the provided computational resources.

References

[1] J.-H. Chen, C. Jang, S. Xiao, M. Ishigami, and M. S. Fuhrer, "Intrinsic and extrinsic performance limits of graphene devices on SiO_2," *Nat. Nanotechnol.*, vol. 3, no. 4, pp. 206–209, Apr. 2008.

[2] X. Li, X. Wang, L. Zhang, S. Lee, and H. Dai, "Chemically derived, ultrasmooth graphene nanoribbon semiconductors," *Science*, vol. 319, no. 5867, pp. 1229–1232, Feb. 2008.

[3] Z. Chen and J. Appenzeller, "Mobility extraction and quantum capacitance impact in high performance graphene field-effect transistor devices," in *IEDM Tech. Dig.*, 2008, pp. 509–512.

[4] X. Wang, Y. Ouyang, X. Li, H. Wang, J. Guo, and H. Dai, "Room-temperature all-semiconducting sub-10 nm graphene nanoribbon field-effect transistors," *Phys. Rev. Lett.*, vol. 100, no. 20, p. 206 803, May 2008.

[5] Y. Yang and R. Murali, "Impact of size effect on graphene nanoribbon transport," *IEEE Electron Device Lett.*, vol. 31, no. 3, pp. 237–239, Mar. 2010.

[6] T. Fang, A. Konar, H. Xing, and D. Jena, "Mobility in semiconducting graphene nanoribbons: Phonon, impurity, and edge roughness scattering," *Phys. Rev. B, Condens. Matter*, vol. 78, no. 20, p. 205 403, Nov. 2008.

[7] M. Bresciani, P. Palestri, and D. Esseni, "Simple and efficient modeling of the E-k relationship and low-field mobility in graphene nano-ribbons," *Solid State Electron.*, vol. 54, no. 9, pp. 1015–1021, Sep. 2010.

[8] D. A. Areshkin, D. Gunlycke, and C. T. White, "Ballistic transport in graphene nanostrips in the presence of disorder: Importance of edge effects," *Nano Lett.*, vol. 7, no. 1, pp. 204–210, Jan. 2007.
[9] D. Querlioz, Y. Apertet, A. Valentin, K. Huet, A. Bournel, S. Galdin-Retailleau, and P. Dollfus, "Suppression of the orientation effects on bandgap in graphene nanoribbons in the presence of edge disorder," *Appl. Phys. Lett.*, vol. 92, no. 4, p. 042 108, Jan. 2008.
[10] A. Betti, G. Fiori, G. Iannaccone, and Y. Mao, "Physical insights on graphene nanoribbon mobility through atomistic simulations," in *IEDM Tech. Dig.*, 2009, pp. 897–900.
[11] G. Iannaccone and M. Pala, "An extended concept of mobility for non diffusive conductors," unpublished.
[12] Code and Documentation. [Online]. Available: http://www.nanohub.org/tools/vides
[13] I. Deretsiz, G. Forte, A. Grassi, A. La Magna, G. Piccitto, and R. Pucci, "A multiscale study of electronic structure and quantum transport in $C_{6n^2}H_{6n}$-based graphene quantum dots," *J. Phys.: Condens. Matter*, vol. 22, no. 9, p. 095 504, Mar. 2010.
[14] K. Rytkönen, J. Akola, and M. Manninen, "Density functional study of alkali metal atoms and monolayers on graphite (0001)," *Phys. Rev. B, Condens. Matter*, vol. 75, no. 7, p. 075 401, Feb. 2007.
[15] P. Michetti and G. Iannaccone, "Analytical model of one-dimensional carbon-based Schottky-barrier transistors," *IEEE Trans. Electron Devices*, vol. 57, no. 7, pp. 1616–1625, Jul. 2010.
[16] Part 1 M. Fischetti, ECE609 Physics of Semiconductor Devices (Spring 2010), p. 80, 2010. [Online]. Available: http://www.ecs.umass.edu/ece/ece609
[17] R. Kotlyar, B. Obradovic, P. Matagne, M. Stettler, and M. D. Giles, "Assessment of room-temperature phonon-limited mobility in gated silicon nanowires," *Appl. Phys. Lett.*, vol. 84, no. 25, pp. 5270–5272, Jun. 2004.
[18] C. Casiraghi, A. Hartschuh, H. Qian, S. Piscanec, C. Georgi, A. Fasoli, K. S. Novoselov, D. M. Basko, and A. C. Ferrari, "Raman spectroscopy of graphene edges," *Nano Lett.*, vol. 9, no. 4, pp. 1433–1441, Apr. 2009.
[19] S. Poli, M. G. Pala, T. Poiroux, S. Deleonibus, and G. Baccarani, "Size dependence of surface-roughness-limited mobility in silicon-nanowire FETs," *IEEE Trans. Electron Devices*, vol. 55, no. 11, pp. 2968–2976, Nov. 2008.
[20] J.-H. Chen, W. G. Cullen, C. Jang, M. S. Fuhrer, and E. D. Williams, "Defect scattering in graphene," *Phys. Rev. Lett.*, vol. 102, no. 23, p. 236 805, Jun. 2009.
[21] M. Evaldsson, I. V. Zozoulenko, H. Xu, and T. Heinzel, "Edge-disorder-induced Anderson localization and conduction gap in graphene nanoribbons," *Phys. Rev. B, Condens. Matter*, vol. 78, no. 16, p. 161 407, Oct. 2008.
[22] T. Stauber, N. M. R. Peres, and F. Guinea, "Electronic transport in graphene: A semiclassical approach including midgap states," *Phys. Rev. B, Condens. Matter*, vol. 76, no. 20, p. 205 423, Nov. 2007.
[23] C. Casiraghi, S. Pisana, K. S. Novoselov, A. K. Geim, and A. C. Ferrari, "Raman fingerprint of charged impurities in graphene," *Appl. Phys. Lett.*, vol. 91, no. 23, p. 233 108, Dec. 2007.
[24] J.-H. Chen, C. Jang, S. Adam, M. S. Fuhrer, E. D. Williams, and M. Ishigami, "Charged-impurity scattering in graphene," *Nat. Phys.*, vol. 4, no. 5, pp. 377–381, May 2008.
[25] E. H. Hwang, S. Adam, and S. Das Sarma, "Carrier transport in two-dimensional graphene layers," *Phys. Rev. Lett.*, vol. 98, no. 18, p. 186 806, May 2007.
[26] K. I. Bolotin, K. J. Sikes, J. Hone, H. L. Stormer, and P. Kim, "Temperature-dependent transport in suspended graphene," *Phys. Rev. Lett.*, vol. 101, no. 9, p. 096 802, Aug. 2008.
[27] J. Lee and H. Spector, "Dielectric response function for a quasi-one-dimensional semiconducting system," *J. Appl. Phys.*, vol. 57, no. 2, pp. 366–372, Jan. 1985.
[28] R. Kubo, "Statistical-mechanical theory of irreversible processes," *J. Phys. Soc. Jpn.*, vol. 12, no. 6, pp. 570–586, Jun. 1957.
[29] D. A. Greenwood, "The Boltzmann equation in the theory of electrical conduction in metals," *Proc. Phys. Soc. London*, vol. 71, no. 4, pp. 585–596, Apr. 1958.
[30] K. M. Borysenko, J. T. Mullen, E. A. Barry, S. Paul, Y. G. Semenov, J. M. Zavada, M. Buongiorno Nardelli, and K. W. Kim, "First-principles analysis of electron–phonon interactions in graphene," *Phys. Rev. B, Condens. Matter*, vol. 81, no. 12, p. 121 412, Mar. 2010.
[31] B. Obradovic, R. Kotlyar, F. Heinz, P. Matagne, T. Rakshit, M. D. Giles, and M. A. Stettler, "Analysis of graphene nanoribbons as a channel material for field-effect transistors," *Appl. Phys. Lett.*, vol. 88, no. 14, p. 142 102, Apr. 2006.
[32] R. S. Shishir and D. K. Ferry, "Intrinsic mobility in graphene," *J. Phys.: Condens. Matter*, vol. 21, no. 23, p. 232 204, Jun. 2009.
[33] M. Lazzeri, S. Piscanec, F. Mauri, A. C. Ferrari, and J. Robertson, "Electron transport and hot phonons in carbon nanotubes," *Phys. Rev. Lett.*, vol. 95, no. 23, p. 236 802, Dec. 2005.
[34] J. L. Manes, "Symmetry-based approach to electron–phonon interactions in graphene," *Phys. Rev. B, Condens. Matter*, vol. 76, no. 4, p. 045430, Jul. 2007.
[35] S. Malola, H. Häkkinen, and P. Koskinen, "Comparison of Raman spectra and vibrational density of states between graphene nanoribbons with different edges," *Eur. Phys. J. D*, vol. 52, no. 1–3, pp. 71–74, Apr. 2009.
[36] A. C. Ferrari, J. C. Meyer, V. Scardaci, C. Casiraghi, M. Lazzeri, F. Mauri, S. Piscanec, D. Jiang, K. S. Novoselov, S. Roth, and A. K. Geim, "Raman spectrum of graphene and graphene layers," *Phys. Rev. Lett.*, vol. 97, no. 18, p. 187 401, Nov. 2006.
[37] A. Akturk and N. Goldsman, "Electron transport and full-band electron–phonon interactions in graphene," *J. Appl. Phys.*, vol. 103, no. 5, p. 053702, Mar. 2008.
[38] V. Perebeinos and P. Avouris, "Inelastic scattering and current saturation in graphene," *Phys. Rev. B, Condens. Matter*, vol. 81, no. 19, p. 195 442, May 2010.
[39] V. Perebeinos, J. Tersoff, and P. Avouris, "Mobility in semiconducting carbon nanotubes at finite carrier density," *Nano Lett.*, vol. 6, no. 2, pp. 205–208, Feb. 2006.
[40] S. Fratini and F. Guinea, "Substrate-limited electron dynamics in graphene," *Phys. Rev. B, Condens. Matter*, vol. 77, no. 19, p. 195 415, May 2008.
[41] A. Konar, T. Fang, and D. Jena, "Effect of high-k gate dielectrics on charge transport in graphene-based field effect transistors," *Phys. Rev. B, Condens. Matter*, vol. 82, no. 11, p. 115 452, Sep. 2010.

Alessandro Betti received the M.S. degree in physics in 2007 from the Università di Pisa, Pisa, Italy, where he is currently working toward the Ph.D. degree in electrical engineering in the Dipartimento di Ingegneria dell'Informazione: Elettronica, Informatica, Telecomunicazioni.

His interests include the transport and noise properties of silicon and carbon quasi-one-dimensional devices.

Gianluca Fiori received the M.S. degree in electrical engineering and the Ph.D. degree from the Università di Pisa, Pisa, Italy, in 2001 and 2005, respectively.

In the autumn of 2002, he visited Silvaco International, developing quantum models, which are currently implemented in the commercial simulator Atlas by Silvaco. In the summer of 2004, 2005, and 2008, he visited Purdue University, West Lafayette, IN, where he worked on models for the simulation of transport in nanoscaled devices. Since December 2007, he has been an Assistant Professor with the Dipartimento di Ingegneria dell'Informazione: Elettronica, Informatica, Telecomunicazioni, Università di Pisa. His main field of activity includes the development of models and codes for the simulations of ultrascaled semiconductor devices. More information available at http://monteverdi.iet.unipi.it/~fiori/.

Giuseppe Iannaccone (M'98–SM'10) received the M.S. and Ph.D. degrees in electrical engineering from the University of Pisa, Pisa, Italy, in 1992 and 1996, respectively.

He was a Researcher with the Italian National Research Council. Since 1996, he has been with the University of Pisa, where he is currently an Associate Professor of electronics. He has published more than 130 papers in peer-reviewed journals and more than 90 papers in proceedings of international conferences. He has coordinated a few European and national projects involving multiple partners and has acted as the Principal Investigator in several research projects funded by public agencies at the European and national levels, and by private organizations. He acts as a Reviewer for a few funding agencies in Europe and is or has been in the technical committee of several international conferences in the field of semiconductor technology and design. His interests include the fundamentals of transport and noise in nanoelectronic and mesoscopic devices, the development of device modeling and technology computer-aided design tools, and the design of extremely low-power circuits and systems for radio-frequency identification and ambient intelligence scenarios. Visit him at www.iannaccone.org/.